Pristine oceans control the uncertainty in aerosol–cloud interactions

Goutam Choudhury[1], Karoline Block[2], Mahnoosh Haghighatnasab[2,3], Johannes Quaas[2], Tom Goren[1], and Matthias Tesche[2]

[1]Department of Environment, Planning and Sustainability, Bar-Ilan University, Ramat Gan, 5290002, Israel
[2]Leipzig Institute for Meteorology, Leipzig University, Leipzig, 04103, Germany
[3]Research and Development, German Weather Service, Offenbach am main, 63067, Germany

Correspondence: Goutam Choudhury (goutam.choudhury@biu.ac.il)

Abstract. Quantifying global cloud condensation nuclei (CCN) concentrations is crucial for reducing uncertainties in radiative forcing resulting from aerosol-cloud interactions. This study analyzes two novel, independent, open-source global CCN datasets derived from spaceborne Cloud Aerosol Lidar with Orthogonal Polarization (CALIOP) measurements and Copernicus Atmosphere Monitoring Service (CAMS) reanalysis and examines the spatio-temporal variability of CCN concentrations pertinent to liquid clouds. The results reveal consistent large-scale patterns in both CALIOP and CAMS datasets, although CALIOP values are approximately 79 % higher than those from CAMS. Comparisons with existing literature demonstrate that these datasets effectively bound the regionally observed CCN concentrations, with CALIOP typically representing the upper bound and CAMS the lower bound. Monthly and annual variations in CCN concentrations obtained from the two datasets largely agree over the Northern Hemisphere and align with previously reported variations. However, inconsistencies emerge over pristine oceans, particularly in the Southern Hemisphere, where the datasets show not only opposing seasonal changes but also contrasting annual trends. A closure study of trends in CCN and cloud droplet concentrations suggests that dust-influenced and pristine-maritime environments primarily limit our current understanding of CCN-cloud-droplet relationships. Long-term CCN observations in these regions are crucial for improving global datasets and advancing our understanding of aerosol-cloud interactions.

1 Introduction

Aerosols act as cloud condensation nuclei (CCN) and through aerosol–cloud interactions (ACI) induce a cooling effect on the climate, partially offsetting the warming due to greenhouse gases (Forster et al., 2021). The effective radiative forcing due to ACI (ERF$_{ACI}$) is however highly uncertain, estimated to range between -1.7 and -0.3 W m^{-2} with moderate confidence (Forster et al., 2021).

A fundamental parameter for constraining ERF$_{ACI}$ is the number concentration of CCN forming aerosols (n_{CCN}). Satellite-based studies of ERF$_{ACI}$ rely on aerosol optical properties as proxies for n_{CCN}. Part of the uncertainty in ERF$_{ACI}$ arises from variations in estimates between different observation-based reports, particularly due to their choice of n_{CCN} proxy (Forster et al., 2021; Gryspeerdt et al., 2017). The most common proxies are aerosol optical depth (AOD) and aerosol index (AI) (Quaas et al., 2020; Rosenfeld et al., 2023). AOD, being a column-integrated bulk property, poorly represents n_{CCN} at cloud

25   level. AI, calculated from AOD and Ångström exponent, gives more weight to fine particles and offers an improvement over AOD. Using AI over AOD strengthens the negative radiative forcing by at least 30 % (Gryspeerdt et al., 2017). Nevertheless, because AI is derived from AOD, it inherits the limitations of AOD (Quaas et al., 2020; Rosenfeld et al., 2023). Incorporating additional polarimetric measurements enables retrievals of atmospheric-column-integrated aerosol number concentrations over oceans, which have been shown to yield a significantly stronger negative forcing compared to AOD and AI (Hasekamp et al.,

30   2019). Despite being a significant improvement over optical proxies, these concentrations are still column-integrated and may not represent the cloud-level values most relevant to ACI. These studies illustrate that ERF_{ACI} significantly varies with the choice of n_{CCN} proxy and highlight the critical need for a comprehensive, height-resolved global n_{CCN} dataset as the next essential step for advancing ERF_{ACI} estimates.

        Two recent efforts have addressed these limitations. Choudhury and Tesche (2023a) present a satellite-derived, vertically-
35   resolved, three-dimensional (3D) dataset of global n_{CCN}. Their approach leverages the Cloud Aerosol Lidar with Orthogonal Polarization (CALIOP) retrievals and employs a validated CCN-retrieval algorithm (Choudhury and Tesche, 2022a) to retrieve n_{CCN} from profiles of aerosol extinction coefficient. The retrieved n_{CCN} are then gridded onto a 2º by 5º latitude-longitude grid with a vertical resolution of 60 m to produce a monthly global n_{CCN} dataset. The robustness of the retrieval algorithm is established through comparisons with in-situ measurements from various land and ocean-based platforms (Choudhury et al.,
40   2022; Choudhury and Tesche, 2022b; Aravindhavel et al., 2023).

        Complementing this effort, Block et al. (2024) present a 3D global n_{CCN} dataset estimated from the Copernicus Atmosphere Monitoring Service (CAMS) aerosol reanalysis (Inness et al., 2019). This dataset is based on a diagnostic box model built on a simplified Kappa-Köhler framework that estimates n_{CCN} from CAMS-derived aerosol mass mixing ratios. It offers a high temporal resolution of one day, a horizontal resolution of 0.75º, and a hybrid sigma-pressure vertical grid with 60 levels. While
45   the validation of this dataset is ongoing, a preliminary comparison to surface-based in-situ observations gives promising results (Block et al., 2024).

        The CAMS n_{CCN} dataset with its high spatio-temporal resolution has great potential for better constraining ERF_{ACI}. However, its dependency on satellite-derived AOD (assimilated into CAMS) and the reliance on modelled aerosol inventories in its simulated component (Inness et al., 2019) necessitates an extensive evaluation to assess the representativeness of this dataset.
50   The CALIOP data's coarse monthly resolution complicates a direct integration into ERF_{ACI} estimation. Nevertheless, it was found to be representative of in-situ measured long-term variations in n_{CCN} at multiple regional continental sites (Choudhury and Tesche, 2022b). Thus, the CALIOP n_{CCN} dataset, currently the only satellite-based 3D global data available, presents a valuable tool for expanding the assessment of the CAMS dataset to a global scale, particularly in regions with limited in-situ observations.

55   Here, we conduct a closure study between the two independent novel n_{CCN} datasets, reconciling not only their variability across diverse spatio-temporal scales but also their co-variability with relevant cloud properties. Furthermore, we augment their validation by comparing their regional concentrations with in-situ measurements from the literature. The comparative analysis bridges the gap between the global datasets, providing insights for their future application and development. Ultimately, this
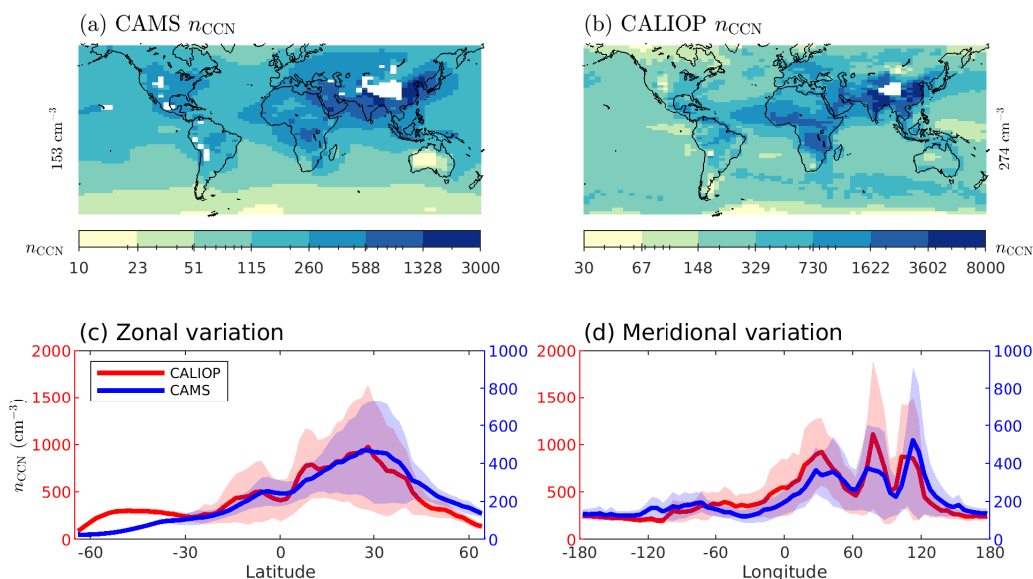
Figure 1. Global climatology of cloud condensation nuclei (CCN) concentration (n_{CCN}) at altitudes below 2 km. (a) Global climatology derived from CAMS reanalysis. (b) Global climatology derived from CALIOP spaceborne lidar. Median n_{CCN} values are displayed on the lateral edges of panels (a) and (b). (c) Zonal variations of n_{CCN} climatology. (d) Meridional variations of n_{CCN} climatology. The semi-transparent patch in (c) and (d) represents one standard deviation. Note the different color scales in top row, and the varying right and left y-axis limits in bottom row.

work aims to establish a benchmark for applying and developing CCN-retrieval algorithms in the context of aerosol-cloud
60 interactions.

2 Results

2.1 n_{CCN} climatology in CAMS and CALIOP

We first compare the spatial variations in n_{CCN} climatology at a supersaturation of 0.20 % for altitudes relevant to liquid clouds (< 2 km) in CALIOP and CAMS datasets (Fig. 1). CAMS n_{CCN} ranges primarily between 28 cm^{-3} and 619 cm^{-3} (5$^{\text{th}}$ and 95$^{\text{th}}$

65 percentiles), with a global median of 153 cm^{-3} (Fig. 1a). In contrast, CALIOP retrievals exhibit a broader range, varying from 107 cm^{-3} to 1445 cm^{-3}, with a global median of 274 cm^{-3} (Fig. 1b). Overall, CALIOP-derived n_{CCN} are approximately 79 % higher than those from CAMS. This difference is also reflected in the magnitudes of their zonal and meridional variations (Fig. 1c and 1d). Despite the discrepancies in magnitudes, the zonal and meridional patterns in both datasets are quite similar, with identical peaks and troughs across most regions except in the Southern Hemisphere (SH). The difference in the SH primarily

70 originates from the retrievals over oceans, where CALIOP-derived concentrations are significantly higher than those from
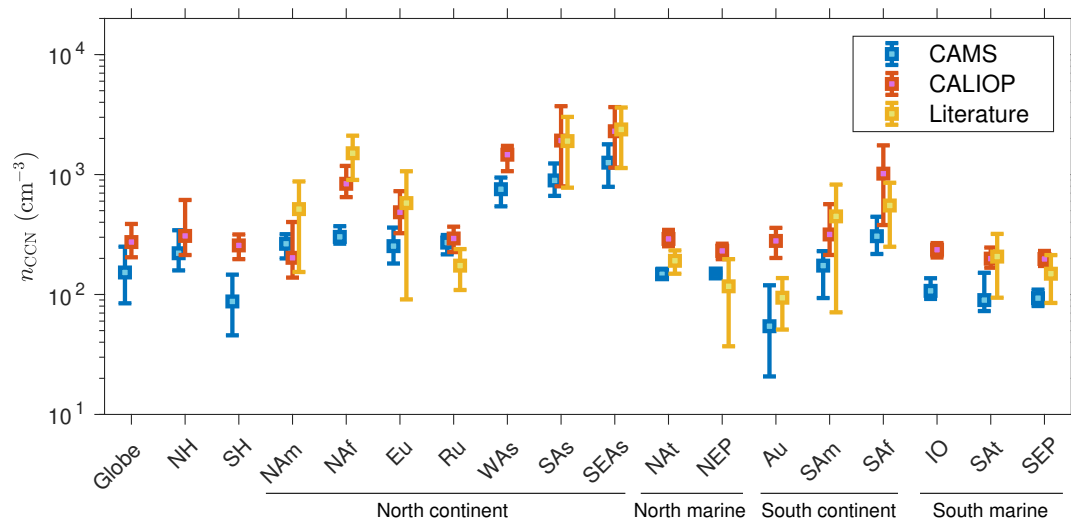
Figure 2. Comparison of regional cloud condensation nuclei (CCN) concentrations n_{CCN} with in-situ measurements. Median n_{CCN} from CAMS reanalysis (blue), CALIOP (red), and in-situ observations from literature (yellow) are compared. Error bars for CAMS and CALIOP represent the geographic interquartile range of n_{CCN}. Error bars for in-situ observations represent the temporal n_{CCN} variations at the specific measurement locations (refer to Table A1). NH: Northern Hemisphere; SH: Southern Hemisphere; NAm: North America; NAf: Northern Africa; Eu: Europe; Ru: Russia; WAs: West Asia; SAs: Southern Asia; SEAs: Southeast Asia; NAt: North Atlantic; NEP: Northeast Pacific; Au: Australia; SAm: South America; SAf: South Africa; IO: Indian Ocean; SAt: South Atlantic; SEP: Southeast Pacific.

CAMS (by 208 %). This difference is particularly large for latitudes below 45° S, where the median CAMS n_{CCN} (33 cm⁻³) is roughly seven times lower than that from CALIOP (263 cm⁻³).

Both datasets show larger n_{CCN} in the Northern Hemisphere (NH) compared to SH. However, this contrast is significantly stronger in CAMS (160 %) compared to CALIOP (20 %). This hemispheric difference in CAMS is particularly pronounced over oceans (121 %) compared to land (59%) and far exceeds the contrast observed in CALIOP (18 % over land and 10 % over oceans). Interestingly, the hemispheric contrast persists in CAMS even over pristine oceans far from continental influence, where CALIOP exhibits homogeneous concentrations. Heterogeneity in CALIOP's oceanic n_{CCN} is primarily related to the transatlantic dust transport in the tropics and the extra-tropical SH region of strong westerly winds. These features are not adequately captured in CAMS retrievals. When comparing the land-ocean n_{CCN} gradients, we find similar values in the NH for both CAMS (65 %) and CALIOP (86 %). However, the gradients in the SH are more pronounced in CAMS (130 %) than CALIOP (73 %) due to its substantially lower concentrations over SH oceans. Refer to Table A1 for the median values used in these calculations

2.1.1 Regional consistency with in-situ observations

To evaluate the datasets, we compare the n_{CCN} climatology from the global datasets with in-situ observations (from the literature, refer Table A1) for 15 regional domains encompassing major continents and ocean basins (geographical boundaries

provided in Fig. A1). Asia exhibits the highest overall n_{CCN} globally (Fig. 2), within which Southeast Asia shows the highest concentration, followed by South Asia and West Asia, consistently across CAMS, CALIOP, and in-situ retrievals. Other continental and oceanic domains follow in decreasing order. Both datasets indicate cleaner SH oceanic regions (Southeast Pacific, South Atlantic, and Indian Ocean) compared to the NH oceans (Northeast Pacific and North Atlantic). However, this hemispheric order is opposite in the in-situ measurements, where concentrations in the SH Atlantic and Pacific oceans exceed their respective NH counterparts. It is important to consider that in-situ observations over oceans are primarily available close to the coast, while the regional domains in this study extend tens of degrees of longitudes away from the coast.

When comparing the magnitudes of n_{CCN}, we observe that CALIOP-derived concentrations are consistently larger than those of CAMS for all regions except North America. These higher values in CALIOP data are expected because the retrieval in CALIOP assumes a fixed CCN-activation radius, above which all aerosols are considered CCN-active regardless of their hygroscopicity. This assumption can lead to large n_{CCN} in urban continental regions (Southeast and South Asia, and Southern Africa) influenced by black carbon and regions downwind. CAMS, on the other hand, considers 80 % of black carbon aerosols to be hydrophobic (not contributing to n_{CCN}) (Block et al., 2024) and excludes dust as a potential CCN source. More details on the inherent differences between the global datasets are discussed in Section A1. Despite these discrepancies, this regional comparison with in-situ measurements suggests that the global datasets adequately capture the observed variations in n_{CCN} climatology for most regions. CALIOP appears to represent the upper bound, while CAMS represents the lower bound of n_{CCN}, highlighting their potential for constraining n_{CCN} even in regions lacking in-situ measurements.

2.2 Monthly n_{CCN} variations

To understand how well the datasets capture the seasonal n_{CCN} cycles, we analyze the average monthly variations in n_{CCN} derived from CALIOP and CAMS for different regional domains (see Fig. 3). Both datasets exhibit a consistent pattern for most continental regions, with n_{CCN} peaking in summer (boreal in NH and austral in SH) and reaching a minimum in winter. This pattern aligns with regional precipitation cycles (shown at the bottom of all panels of Fig. 3). Wet winters lead to precipitation scavenging of airborne particles, resulting in lower n_{CCN} compared to dry summers. Exceptions are the monsoon-influenced South and Southeast Asia, which experience a summer minimum and winter maximum in n_{CCN} due to prolonged summer rainfall. Both datasets adequately capture this seasonal pattern driven by the monsoon cycle.

However, the datasets show contrasting variations for all oceanic regions except North Atlantic ocean. CALIOP exhibits a summer minimum and winter maximum in oceanic n_{CCN}, while CAMS mostly shows a spring maximum and winter minimum. The variations in CALIOP align with the seasonal cycle of near-surface wind speeds over oceans (Yu et al., 2020). Higher wind speeds increase sea spray aerosol concentrations in marine environments by enhancing wave breaking and bubble bursting (Revell et al., 2019; Humphries et al., 2023). This could potentially contribute to the observed CCN cycles in CALIOP. However, oceanic n_{CCN} is influenced by factors beyond sea spray aerosols, such as biogenic emissions, whose monthly variations (Revell et al., 2019) are more similar to those of CAMS. Due to limited in-situ observations, it is currently unclear how much each of these factors contribute to the total oceanic n_{CCN}. It is important to note that the SH oceans are the primary contributor to global low-level cloud cover (see bottom of all panels in Fig. 3, and Fig. A2). The inconsistency between the
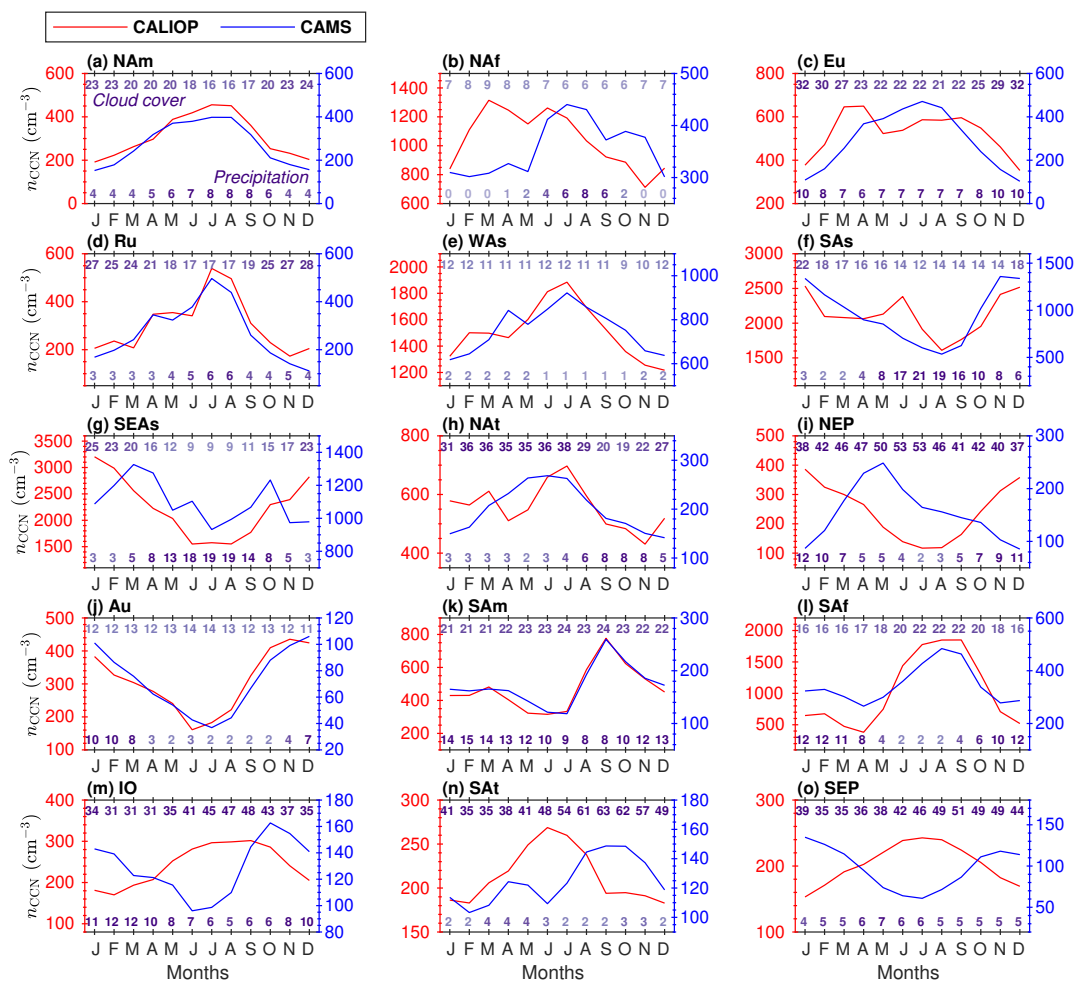
Figure 3. Monthly variations in cloud condensation nuclei concentrations (n_{CCN}) for various regions. Red lines represent n_{CCN} derived from spaceborne CALIOP, and blue lines represent n_{CCN} from CAMS reanalysis. Panels (a) to (i) (top three rows) correspond to Northern Hemisphere regions, while panels (j) to (o) (bottom two rows) represent Southern Hemisphere regions. Note the separate y-axes for CALIOP (left) and CAMS (right). The numbers at the top and bottom of each panel represent the monthly climatology of low cloud cover (in %) from CERES and precipitation (in cm) from GPCP product, respectively, with the opacity of the numbers proportional to their magnitude. NAm: North America; NAf: Northern Africa; Eu: Europe; Ru: Russia; WAs: West Asia; SAs: Southern Asia; SEAs: Southeast Asia; NAt: North Atlantic; NEP: Northeast Pacific; Au: Australia; SAm: South America; SAf: South Africa; IO: Indian Ocean; SAt: South Atlantic; SEP: Southeast Pacific.

120   global n_{CCN} datasets in these cloud-rich regions, which are crucial for ACI, raises significant questions and challenges for their use in quantifying these interactions.

6
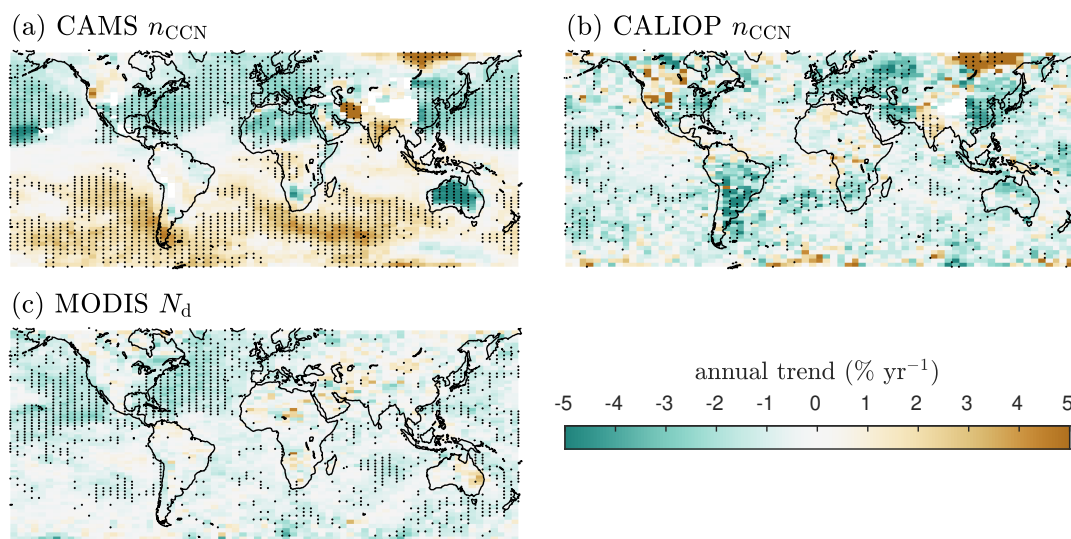
Figure 4. Comparison of global trends computed using annual time series. (a) Trends in cloud condensation nuclei concentrations (n_{CCN}) derived from CAMS reanalysis. (b) Trends in n_{CCN} from CALIOP. (c) Trends in cloud droplet number concentrations (N_{d}) derived from MODIS. Dots in each panel indicate the grids where the trend is statistically significant. The absolute values of the trends are shown in Fig. A3.

2.3 Reconciling trends in n_{CCN} and N_{d}

Quantifying trends in n_{CCN} is crucial for comprehending the present dynamics of radiative forcing due to ACI and for projecting future changes. Recent decades have witnessed declining aerosol emission rates and aerosol loadings over land (Col-
125 laud Coen et al., 2020; Quaas et al., 2022) and oceans (IMO, 2019; Gryspeerdt et al., 2019) due to stricter emission policies. An exception is the South Asia region, where aerosol emissions have been increasing in the 21$^{\mathrm{st}}$ century (Jin et al., 2023). These emission trends are also expected to be reflected in cloud droplet number concentrations (N_{d}) because of their strong sensitivity to changes in n_{CCN} (McCoy et al., 2018; Quaas et al., 2022). Therefore, we expect the annual trends in n_{CCN} and N_{d} to be similar to the emission trends.

130 Over NH regions, the emission trends are reflected in both the n_{CCN} datasets (Figs. 4a and 4b). As expected, all regions except South Asia exhibit a declining n_{CCN} trend (see Fig. 5 and Table A1). The trends in N_{d} are also consistent with those in n_{CCN} from both CALIOP and CAMS (Fig. 5), with exceptions only observed over dust-influenced regions (Northern Africa and West Asia). This discrepancy may be attributed to the hydrophobic nature of fresh mineral dust, which may not readily act as CCN due to a lack of mixing or coating with water-soluble aerosols (Garimella et al., 2014).

135 Over SH regions, CALIOP shows declining n_{CCN} trends across all domains. N_{d} trends are mostly negative as well consistent with CALIOP, except for dust-influenced Australia (Au) domain. Of particular interest are the spatially uniform and statistically significant increasing trends in CAMS-derived n_{CCN} at altitudes below 2 km over most SH oceanic regions. This finding not only contradicts the negative trend observed in N_{d} and CALIOP-derived n_{CCN} but also the expected decreasing trend inferred
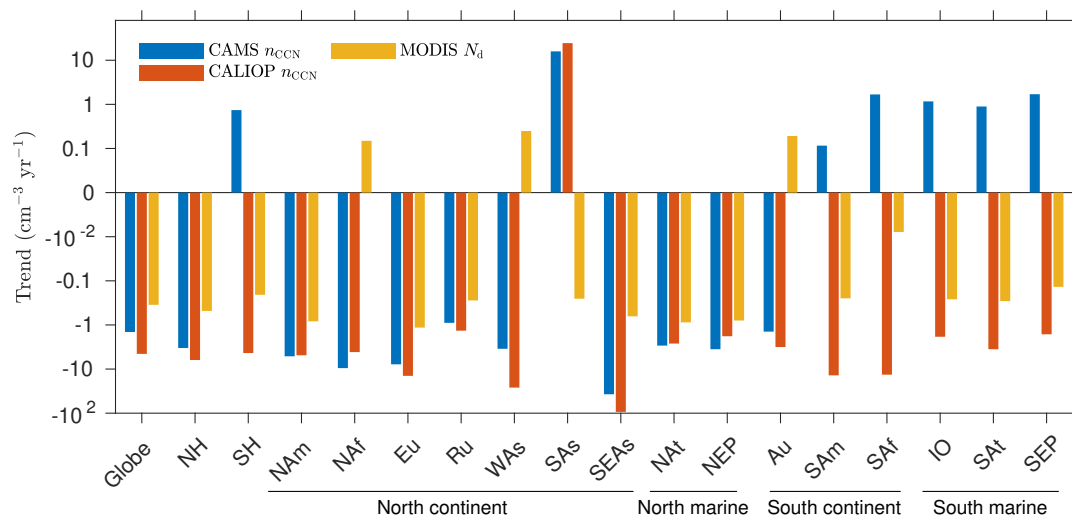
Figure 5. Comparison of regional trends computed using annual time series. Trends (in cm^{-3} yr^{-1}) in cloud condensation nuclei concentrations (n_{CCN}) derived from CAMS reanalysis (blue), trends in n_{CCN} from CALIOP (red), and trends in N_{d} from MODIS (yellow) are compared. NH: Northern Hemisphere; SH: Southern Hemisphere; NAm: North America; NAf: Northern Africa; Eu: Europe; Ru: Russia; WAs: West Asia; SAs: Southern Asia; SEAs: Southeast Asia; NAt: North Atlantic; NEP: Northeast Pacific; Au: Australia; SAm: South America; SAf: South Africa; IO: Indian Ocean; SAt: South Atlantic; SEP: Southeast Pacific.

from previous ship emission reports (Quaas et al., 2022). It is worth noting that the increasing SH n_{CCN} trends in CAMS

140   coincide with trends in AOD derived from MODIS (Fig. A4). Since MODIS AOD is used to constrain the CAMS aerosol reanalysis (Inness et al., 2019), a proportionality between AOD and CAMS-derived n_{CCN} is inherent in homogeneous marine environments (Block et al., 2024), and may contribute to the observed increasing trends in CAMS. These inconsistencies over pristine oceans, where the trends in aerosol loadings differ between different spaceborne retrievals (Quaas et al., 2022), question the representativeness of the n_{CCN} and N_{d} retrievals, making it challenging to derive their inter-relationship, a parameter key

145   to quantifying ACI.

3   Conclusions

The closure study presented here shows good consistency between the independent CALIOP and CAMS global n_{CCN} datasets in the NH. However, discrepancies emerge over pristine SH oceans not only in the n_{CCN} climatology but also in their monthly and annual variations. Further compounding the challenge, CAMS exhibits anomalous increasing n_{CCN} trend over the SH

150   oceans, which aligns with trends in AOD but contradicts the observed variations in CALIOP as well as in N_{d}. This geographically limited disagreement, restricted to pristine oceans which lack in-situ measurements, raises questions about the adequacy of aerosol inventories used by CAMS over the SH oceans, a known issue in climate models (Moore et al., 2013). Such discrep-

ancies in cloud-rich pristine oceans are particularly concerning because cloud properties in these regions are highly sensitive to even small perturbations in aerosol concentrations (Moore et al., 2013; Gryspeerdt et al., 2021).

155 In conclusion, the aerosol-limited environments of SH oceans are identified as a significant source of uncertainty in the present effort to quantify a highly resolved global n_{CCN} dataset. Future research efforts should therefore focus on accurately quantifying the sources of CCN and their long-term cycles in remote SH oceans. These efforts are crucial to refine the global n_{CCN} datasets and ultimately to reduce the uncertainties in $\mathrm{ERF_{ACI}}$.

Appendix A: Methods

170 A1 Global n_{CCN} datasets

CALIOP dataset provides n_{CCN} at a supersaturation of 0.20 %. It is available on a uniform latitude-longitude grid of resolution 2º by 5º, a vertical grid resolution of 60 m extending from mean sea level to a height of 8 km above mean sea level, and a temporal resolution of one month. The dataset is derived from more than 15 years of CALIOP level 2 aerosol profile product from June 2006 to December 2021. It is based on a CCN-retrieval algorithm (Choudhury and Tesche, 2022a) that integrates the 175 CALIOP-derived height-resolved information on the aerosol-type-specific extinction coefficient and microphysical properties from CALIOP's aerosol model with the optical modelling capabilities of the MOPSMAP (Modelled Optical Properties of enseMbles of Aerosol Particles; Gasteiger and Wiegner, 2018) package. Essentially, the algorithm adjusts the normalized size distributions within the aerosol model to match the extinction coefficient. These adjusted size distributions are then used to estimate particle number concentrations relevant for CCN activation. Aerosol-type-specific CCN parameterizations are then 180 applied to calculate n_{CCN} at a supersaturation of 0.20 % for continental (comprising of clean, polluted, and smoke aerosols), dust, and marine aerosols. The algorithm accounts for hygroscopic growth of hydrophilic aerosols (continental and marine aerosols) under humid conditions using the κ-parameterization within MOPSMAP package. Evaluations of the algorithm have demonstrated good agreement with independent ground-based and airborne in-situ measurements across diverse geographic

locations, with a combined normalized mean bias of ≈ 22 % and a normalized absolute error of ≈ 61 % (Choudhury et al.,
2022; Choudhury and Tesche, 2022b; Aravindhavel et al., 2023; Choudhury and Tesche, 2023a). The resulting CALIOP-
derived n_{CCN} has also been utilized in quantifying the CCN activation ratio for liquid clouds (Alexandri et al., 2023).

CAMS n_{CCN} dataset is derived from CAMS aerosol reanalysis of mass mixing ratios (Block et al., 2024) and provides
n_{CCN} at supersaturations ranging from 0.1 % to 1 %. The dataset is available on a uniform horizontal grid of resolution 0.75º
by 0.75º and a vertical grid with 60 hybrid sigma–pressure levels extending from the surface to 0.1 hPa. The CCN-retrieval
algorithm in CAMS utilizes a box-model framework (O'Connor et al., 2014; West et al., 2014) to convert the mass mixing ratios
of five aerosols species—sulfate, mineral dust, black carbon (hydrophobic and hydrophilic), organic matter (hydrophobic and
hydrophilic), and sea salt—into total number concentrations. Subsequently, these concentrations are combined with normalized
size distributions derived from the aerosol module of the European Centre for Medium-Range Weather Forecasts (ECMWF)
Integrated Forecasting System (IFS) model (Benedetti et al., 2009) to estimate the actual aerosol size distribution. The size
distributions of hydrophillic aerosols are then coupled with auxillary meteorological parameters and used in modified Kappa-
Köhler theory (Pöhlker et al., 2023) to calculate the activated n_{CCN} at various supersaturations. Consistent with the CAMS
model's assumption of completely hydrophobic dust with no consideration of internal mixing or external coating mechanisms,
dust is excluded in the CCN calculations. Initial validation results using surface in-situ CCN observations at continental and
coastal Atmospheric Radiation Measurement (ARM) network sites have shown promising results, with an acceptable bias
factor of 1.29 (Block et al., 2024).

A1.1 Limitations of n_{CCN} datasets

CALIOP n_{CCN} dataset is subject to uncertainties arising from errors in the underlying CALIOP products and approximations
within the CCN-retrieval algorithm. Uncertainties in CALIOP extinction coefficients can reach 30 %. Assuming fixed aerosol-
type-specific size distributions introduces additional uncertainty, estimated to be a factor of 1.5–2 (Choudhury and Tesche,
2022a). Further, the algorithm assumes an aerosol-species dependent fixed CCN activation radius (50 nm for continental and
marine aerosols, and 100 nm for mineral dust at a supersaturation of 0.20 %). Using a fixed CCN activation size (assuming
all larger particles are CCN active) may result in about a 20 % overestimation in the final CCN product (Choudhury and
Tesche, 2022b). Accounting for all these limitations, the overall uncertainty associated with the CALIOP-derived CCN dataset
is expected to be a factor of 2–3 (Choudhury and Tesche, 2023a). Moreover, the CALIOP dataset is produced using only
cloud-free aerosol profiles. This can lead to sampling bias in regions with significant cloud cover, potentially leading to the
differences observed between the CALIOP and CAMS datasets. However, there appears to be no clear relationship between
the correlation of the CALIOP and CAMS n_{CCN} datasets and the sampling frequency of CALIOP (Fig. A5).

Similarly, uncertainties in CAMS n_{CCN} dataset may stem from the source CAMS aerosol reanalysis product and the CCN-
estimation methodology. CAMS aerosol product is constrained by satellite-derived AOD retrievals, particularly the MODIS
dark target and deep blue AOD retrievals at 0.55 um (Platnick et al., 2017b) and Advanced Along-Track Scanning Radiome-
ter (AATSR) retrieved AOD (Popp et al., 2016). Therefore, uncertainties in AOD retrievals can propagate into the CAMS
reanalysis and ultimately the n_{CCN} product. Additionally, missing aerosol sources in the CAMS emission inventory (Moore

et al., 2013; Errera et al., 2021) can introduce uncertainties, especially in remote areas with sparse observations, limiting the effectiveness of emission parameterizations implemented in the aerosol model. Furthermore, unlike the approach in CALIOP,

220 the CAMS-based retrieval excludes mineral dust. Studies have demonstrated that mineral dust may be a potential CCN source, particularly when coated or internally mixed with water-soluble hydrophilic aerosols (Kumar et al., 2009; Bègue et al., 2015). This exclusion may thus lead to an underestimation in the final n_{CCN} product.

A2 Spaceborne cloud and precipitation data

N_{d} data for low-level liquid clouds are derived from the Moderate Resolution Imaging Spectroradiometer (MODIS) aboard

225 Aqua polar orbiting satellite (Gryspeerdt et al., 2022). The dataset is available at a uniform spatial resolution of 1° by 1° with daily temporal resolution spanning from July 2002 and 2020. Low-level cloud cover data are obtained from the Clouds and the Earth's Radiant Energy System (CERES) SYN Edition 4A monthly product (Doelling et al., 2013). This product merges retrievals from CERES, MODIS, and geostationary sensors to construct a global gridded dataset suitable for studying aerosol-cloud interactions. The dataset is operationally available at a latitude-longitude resolution of 1° by 1° starting from July 2002.

230   Precipitation data are derived from the Global Precpitation Climatology Project (GPCP) monthly product (Adler et al., 2003). This product integrates rainfall data obtained from several platforms, including satellites, in-situ soundings, and rain gauges, to generate a global monthly precipitation dataset on a uniform horizontal resolution of 2.5 $^{\mathrm{o}}$ available from 1979.

A3 Data harmonization, trend estimation, and averaging methodologies

CCN, cloud, and precipitation parameters are considered between latitudes of 65° N and 65°S. Horizontal grids of all datasets

235 are harmonized by transforming them to the coarser 2° by 5° latitude-longitude grid of CALIOP using bilinear interpolation. We exclude CAMS data in grids surrounding Mauna Loa and Altzomoni due to documented biases in CAMS aerosol emission datasets over these regions (Inness et al., 2019).

  To specifically focus on the liquid clouds, which are most relevant for aerosol-cloud interactions, average n_{CCN} between altitudes of 0–2 km are considered in this study. Additionally, a supersaturation of 0.20 % is selected because this value

240 represents a characteristic supersaturation near the base of liquid clouds. Temporal averages of CALIOP data are weighted by the number of valid aerosol retrievals within each grid cell (Choudhury and Tesche, 2023a). Horizontal averages in CALIOP and CAMS are weighted by the area of the latitude-longitude grids. Trends in n_{CCN} and N_{d} are estimated using the non-parametric Mann-Kendall trend. Monthly and annual statistics are calculated using data between 2007 and 2021 for CALIOP-and CAMS-derived n_{CCN}, and between 2007 and 2020 for MODIS-derived N_{d}.
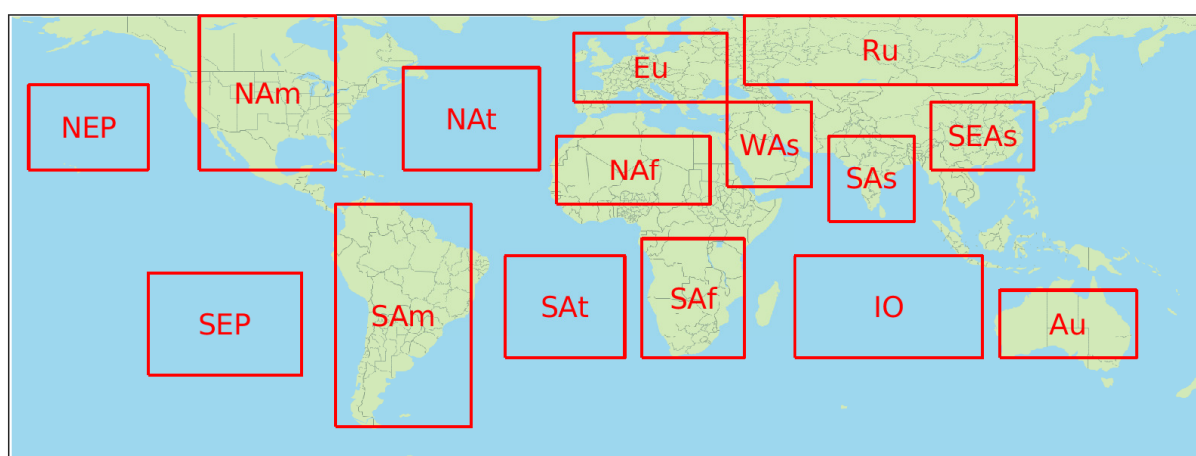
Figure A1. Regional domains considered in this study. NAm: North America $[20° − 65°N, 120° − 80°W]$; NAf: Northern Africa $[10° − 30°N, 15°W − 30°E]$; Eu: Europe $[40° − 60°N, 10°W − 35°E]$; Ru: Russia $[45° − 65°N, 40° − 120°E]$; WAs: West Asia $[15° − 40°N, 35° − 60°E]$; SAs: Southern Asia $[5° − 30°N, 65° − 90°E]$; SEAs: Southeast Asia $[20° − 40°N, 95° − 125°E]$; NAt: North Atlantic $[10° − 35°N, 60° − 20°W]$; NEP: Northeast Pacific $[20° − 45°N, 170° − 135°W]$; Au: Australia $[35° − 15°S, 115° − 155°E]$; SAm: South America $[55° − 10°S, 80° − 40°W]$; SAf: South Africa $[35° − 0°S, 10° − 40°E]$; IO: Indian Ocean $[35° − 5°S, 55° − 110°E]$; SAt: South Atlantic $[35° − 5°S, 30°W − 5°E]$; SEP: Southeast Pacific $[40° − 10°S, 135° − 90°W]$.
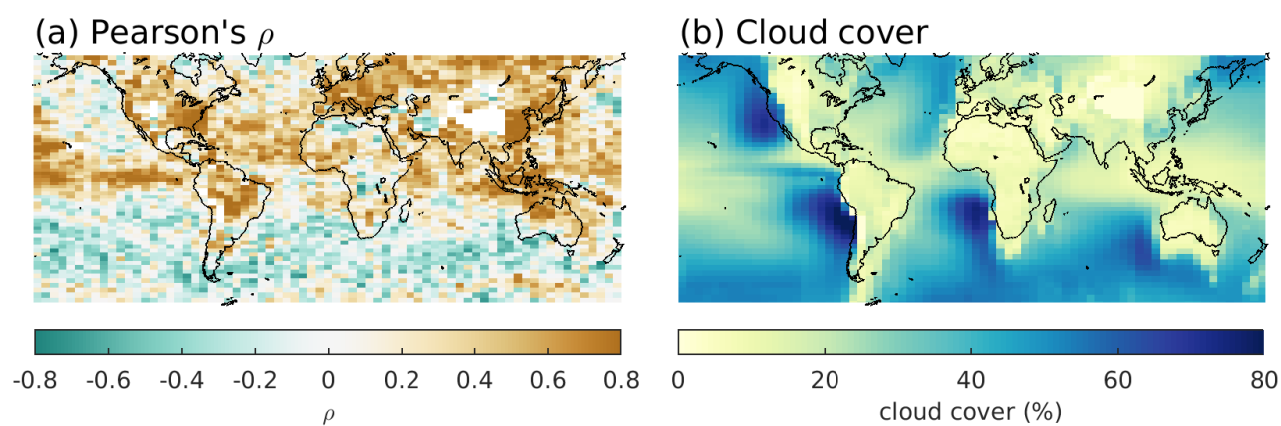
Figure A2. Relating correlation between CALIOP and CAMS with global cloud cover. Panel (a): Global map of Pearson's correlation coefficient (ρ) between monthly mean cloud condensation nuclei concentration (n_{CCN}) derived from spaceborne CALIOP and CAMS reanalysis datasets. Panel (b): Low-level cloud cover climatology (in %) derived from CERES SYN product.
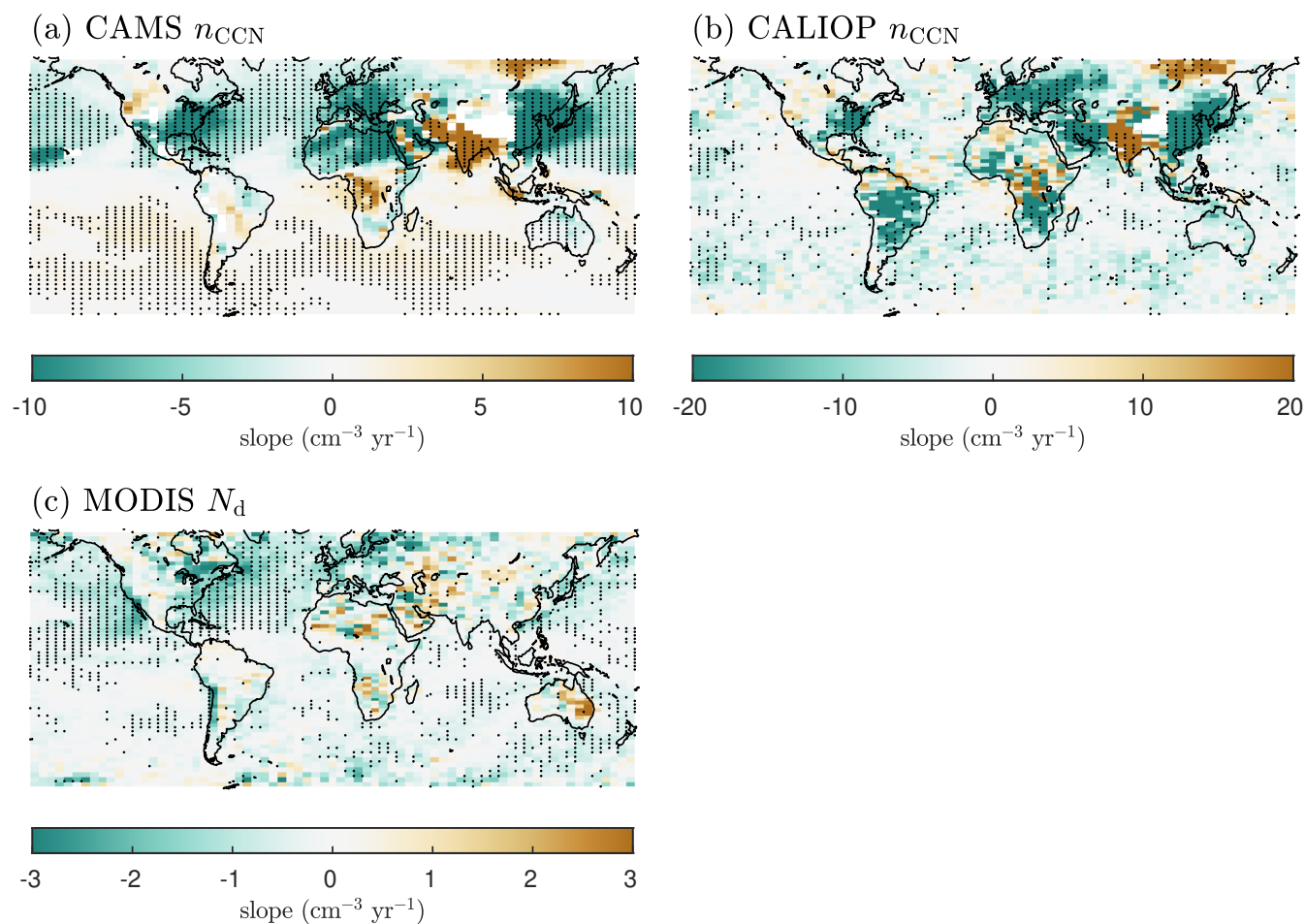
Figure A3. Comparison of global trends (in cm^{-3} yr^{-1}) computed using annual time series. (a) Trends in cloud condensation nuclei concentrations (n_{CCN}) derived from CAMS reanalysis. (b) Trends in n_{CCN} from CALIOP. (a) and spaceborne CALIOP. (c) Trends in cloud droplet number concentrations (N_{d}) derived from MODIS. Dots in each panel indicate the grids where the trend is statistically significant. Figure with trends in percentages are shown in Fig. 4 of the manuscript.
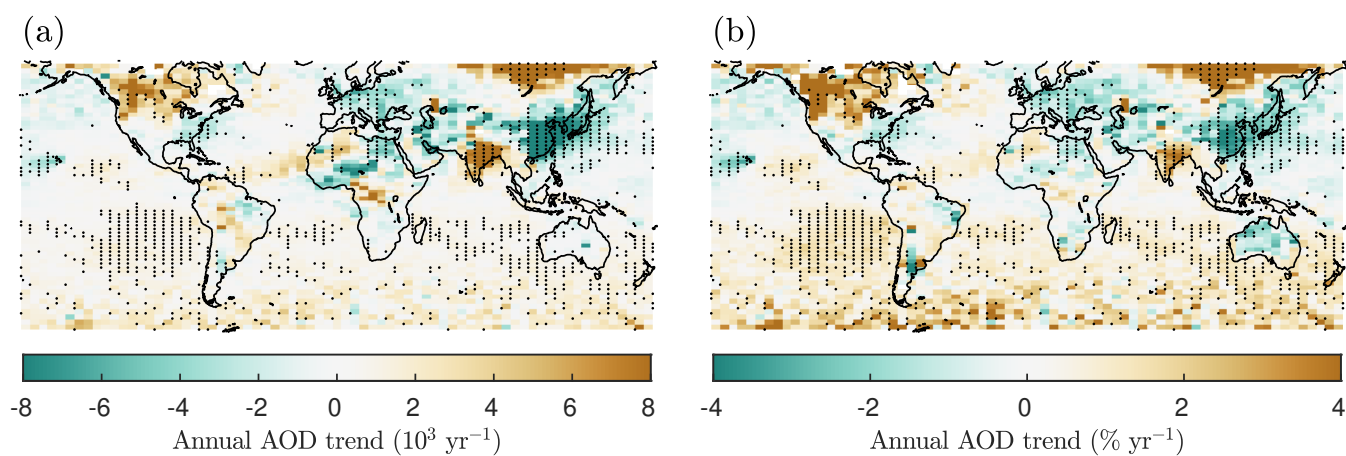
Figure A4. Global map of annual trend in MODIS AOD derived using combined dark target and deep blue algorithms. Panel (a) shows the trend in 10^3 yr^{-1} and panel (b) in % yr^{-1}. Dots in each panel indicate the grids where the trend is statistically significant.
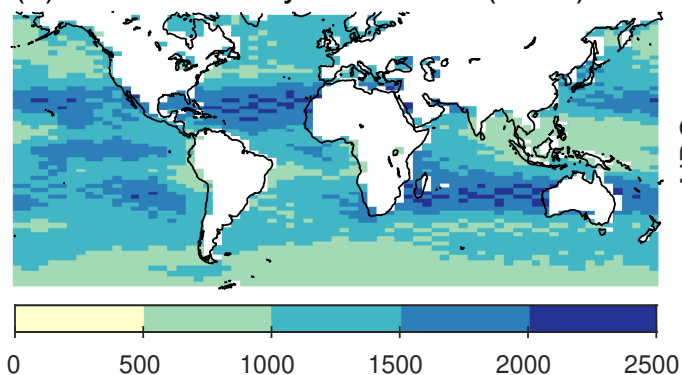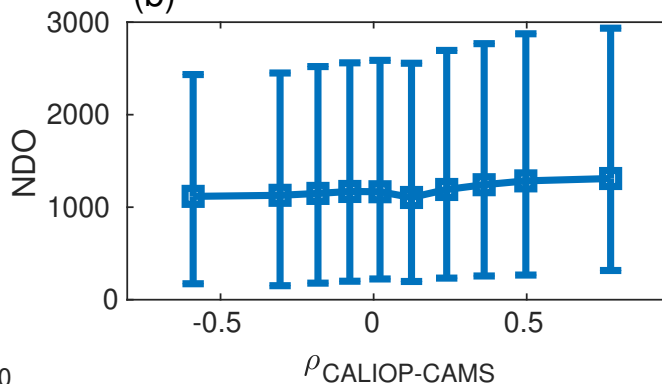
Figure A5. Relationship between sampling frequency in CALIOP and correlation between the datasets. (a) Global map of number of days with a valid aerosol retrieval observed by CALIOP within period of June 2006 to December 2021. (b) Median number of valid CALIOP aerosol retrieval over oceans observed versus Pearson's correlation coefficient between CALIOP and CAMS ($\rho_{\mathrm{CALIOP-CAMS}}$). Error bars denote the interquartile range. Each $\rho_{\mathrm{CALIOP-CAMS}}$ bin consists of 407 data points.

Table A1. Median cloud condensation nuclei (CCN) concentration (n_{CCN}) at a supersaturation of 0.20 % in cm^{-3} with interquartile range in parentheses, and annual n_{CCN} trend in cm^{-3} yr^{-1} for various regions. Trends in bold indicate statistically significant trends ($p < 0.05$). In-situ n_{CCN} observations and their corresponding references are also provided. Abbreviations are explained in the footnote.

Region	CALIOP n_{CCN}	Trend CALIOP	CAMS n_{CCN}	Trend CAMS	In situ n_{CCN}	In-situ reference
Globe	274 (204, 387)	**-4.5**	153 (84, 250)	**-1.4**	-	-
Land	483 (230, 1071)	**-3.5**	276 (188, 398)	**-1**	-	-
Ocean	259 (200, 322)	**-1.9**	130 (71, 183)	**-0.5**	-	-
NH	308 (213, 614)	**-6.2**	221 (159, 343)	**-3.3**	-	-
NH land	510 (225, 1143)	**-4.4**	296 (214, 447)	**-1.8**	-	-
NH ocean	275 (212, 395)	**-2**	179 (147, 267)	**-1.9**	-	-
SH	257 (198, 315)	**-4.3**	85 (44, 139)	**0.7**	-	-
SH land	432 (245, 831)	**-2.5**	186 (91, 276)	0	-	-
SH ocean	250 (194, 299)	**-2.1**	81 (41, 124)	**0.8**	-	-
NAm	202 (138, 402)	**-4.9**	265 (200, 318)	**-5.1**	515 (154, 876)	Shen et al. (2019)
NAf	837 (648, 1180)	-4.1	302 (265, 371)	**-9.5**	1505 (902, 2108)	Désalmand (1987)
Eu	485 (324, 726)	**-14.2**	253 (181, 361)	**-7.8**	578 (91, 1065)	Paramonov et al. (2015)
Ru	293 (226, 367)	-1.3	271 (216, 313)	-0.9	174 (109, 239)	Asmi et al. (2016)
WAs	1464 (1066, 1734)	**-26.3**	755 (543, 944)	-3.5	-	-
SAs	1920 (798, 3713)	**24.4**	893 (664, 1237)	**15.9**	1900 (777, 3023)	Jayachandran et al. (2020)
SEAs	2297 (1142, 3649)	**-93.5**	1256 (790, 1787)	**-37.3**	2377 (1133, 3023)	Shen et al. (2019)
NAt	291 (252, 346)	-2.6	147 (138, 164)	**-2.9**	191 (149, 233)	Wood et al. (2017)
NEP	231 (197, 265)	-1.8	150 (146, 155)	**-3.5**	117 (37, 197)	Brendecke et al. (2022)
Au	280 (202, 359)	-3.2	54 (21, 119)	**-1.4**	94 (51, 137)	Humphries et al. (2023)
SAm	317 (213, 566)	**-13.9**	174 (93, 230)	0.1	448 (71, 825)	Shen et al. (2019)
SAf	1017 (379, 1751)	**-13.4**	306 (218, 445)	1.7	552 (250, 854)	Ross et al. (2003)
IO	236 (203, 268)	**-1.9**	107 (92, 137)	**1.2**	-	-
SAt	199 (167, 246)	**-3.6**	90 (73, 152)	**0.9**	207 (94, 320)	Redemann et al. (2021)
SEP	198 (173, 231)	**-1.6**	93 (80, 110)	**1.7**	149 (85, 213)	Allen et al. (2011)

NH: Northern Hemisphere; SH: Southern Hemisphere; NAm: North America; NAf: Northern Africa; Eu: Europe; Ru: Russia; WAs: West Asia; SAs: Southern Asia; SEAs: Southeast Asia; NAt: North Atlantic; NEP: Northeast Pacific; Au: Australia; SAm: South America; SAf: South Africa; IO: Indian Ocean; SAt: South Atlantic; SEP: Southeast Pacific

References

Adler, R. F., Huffman, G. J., Chang, A., Ferraro, R., Xie, P.-P., Janowiak, J., Rudolf, B., Schneider, U., Curtis, S., Bolvin, D., Gruber, A., Susskind, J., Arkin, P., and Nelkin, E.: The Version-2 Global Precipitation Climatology Project (GPCP) Monthly Precipitation Analysis (1979–Present), Journal of Hydrometeorology, 4, 1147 – 1167, https://doi.org/10.1175/1525-7541(2003)004<1147:TVGPCP>2.0.CO;2, 2003.

Alexandri, F., Müller, F., Choudhury, G., Achtert, P., Seelig, T., and Tesche, M.: A cloud-by-cloud approach for studying aerosol-cloud interaction in satellite observations, EGUsphere, 2023, 1–31, https://doi.org/10.5194/egusphere-2023-2773, 2023.

Allen, G., Coe, H., Clarke, A., Bretherton, C., Wood, R., Abel, S. J., Barrett, P., Brown, P., George, R., Freitag, S., McNaughton, C., Howell, S., Shank, L., Kapustin, V., Brekhovskikh, V., Kleinman, L., Lee, Y.-N., Springston, S., Toniazzo, T., Krejci, R., Fochesatto, J., Shaw, G., Krecl, P., Brooks, B., McMeeking, G., Bower, K. N., Williams, P. I., Crosier, J., Crawford, I., Connolly, P., Allan, J. D., Covert, D., Bandy, A. R., Russell, L. M., Trembath, J., Bart, M., McQuaid, J. B., Wang, J., and Chand, D.: South East Pacific atmospheric composition and variability sampled along 20° S during VOCALS-REx, Atmospheric Chemistry and Physics, 11, 5237–5262, https://doi.org/10.5194/acp-11-5237-2011, 2011.

Aravindhavel, A., Choudhury, G., Prabhakaran, T., Murugavel, P., and Tesche, M.: Retrieval and validation of cloud condensation nuclei from satellite and airborne measurements over the Indian Monsoon region, Atmospheric Research, 290, 106 802, https://doi.org/https://doi.org/10.1016/j.atmosres.2023.106802, 2023.

Asmi, E., Kondratyev, V., Brus, D., Laurila, T., Lihavainen, H., Backman, J., Vakkari, V., Aurela, M., Hatakka, J., Viisanen, Y., Uttal, T., Ivakhov, V., and Makshtas, A.: Aerosol size distribution seasonal characteristics measured in Tiksi, Russian Arctic, Atmospheric Chemistry and Physics, 16, 1271–1287, https://doi.org/10.5194/acp-16-1271-2016, 2016.

Bègue, N., Tulet, P., Pelon, J., Aouizerats, B., Berger, A., and Schwarzenboeck, A.: Aerosol processing and CCN formation of an intense Saharan dust plume during the EUCAARI 2008 campaign, Atmospheric Chemistry and Physics, 15, 3497–3516, https://doi.org/10.5194/acp-15-3497-2015, 2015.

Benedetti, A., Morcrette, J.-J., Boucher, O., Dethof, A., Engelen, R. J., Fisher, M., Flentje, H., Huneeus, N., Jones, L., Kaiser, J. W., Kinne, S., Mangold, A., Razinger, M., Simmons, A. J., and Suttie, M.: Aerosol analysis and forecast in the European Centre for Medium-Range Weather Forecasts Integrated Forecast System: 2. Data assimilation, Journal of Geophysical Research: Atmospheres, 114, https://doi.org/https://doi.org/10.1029/2008JD011115, 2009.

Block, K.: Cloud condensation nuclei (CCN) numbers derived from CAMS reanalysis EAC4 (Version 1), https://doi.org/10.26050/WDCC/QUAERERE_CCNCAMS_v1, 2023.

Block, K., Haghighatnasab, M., Partridge, D. G., Stier, P., and Quaas, J.: Cloud condensation nuclei concentrations derived from the CAMS reanalysis, Earth System Science Data, 16, 443–470, https://doi.org/10.5194/essd-16-443-2024, 2024.

Brendecke, J., Dong, X., Xi, B., and Zheng, X.: Maritime Aerosol and CCN Profiles Derived From Ship-Based Measurements Over Eastern North Pacific During MAGIC, Earth and Space Science, 9, e2022EA002 319, https://doi.org/10.1029/2022EA002319, 2022.

Choudhury, G. and Tesche, M.: Estimating cloud condensation nuclei concentrations from CALIPSO lidar measurements, Atmospheric Measurement Techniques, 15, 639–654, https://doi.org/10.5194/amt-15-639-2022, 2022a.

Choudhury, G. and Tesche, M.: Assessment of CALIOP-Derived CCN Concentrations by In Situ Surface Measurements, Remote Sensing, 14, https://doi.org/10.3390/rs14143342, 2022b.

Choudhury, G. and Tesche, M.: A first global height-resolved cloud condensation nuclei data set derived from spaceborne lidar measurements, Earth System Science Data, 15, 3747–3760, https://doi.org/10.5194/essd-15-3747-2023, 2023a.

295 Choudhury, G. and Tesche, M.: Global multiyear 3D dataset of cloud condensation nuclei derived from spaceborne lidar measurements., https://doi.org/10.1594/PANGAEA.956215, 2023b.

Choudhury, G., Ansmann, A., and Tesche, M.: Evaluation of aerosol number concentrations from CALIPSO with ATom airborne in situ measurements, Atmospheric Chemistry and Physics, 22, 7143–7161, https://doi.org/10.5194/acp-22-7143-2022, 2022.

Collaud Coen, M., Andrews, E., Alastuey, A., Arsov, T. P., Backman, J., Brem, B. T., Bukowiecki, N., Couret, C., Eleftheriadis, K., Flentje,
300 H., Fiebig, M., Gysel-Beer, M., Hand, J. L., Hoffer, A., Hooda, R., Hueglin, C., Joubert, W., Keywood, M., Kim, J. E., Kim, S.-W., Labuschagne, C., Lin, N.-H., Lin, Y., Lund Myhre, C., Luoma, K., Lyamani, H., Marinoni, A., Mayol-Bracero, O. L., Mihalopoulos, N., Pandolfi, M., Prats, N., Prenni, A. J., Putaud, J.-P., Ries, L., Reisen, F., Sellegri, K., Sharma, S., Sheridan, P., Sherman, J. P., Sun, J., Titos, G., Torres, E., Tuch, T., Weller, R., Wiedensohler, A., Zieger, P., and Laj, P.: Multidecadal trend analysis of in situ aerosol radiative properties around the world, Atmospheric Chemistry and Physics, 20, 8867–8908, https://doi.org/10.5194/acp-20-8867-2020, 2020.

305 Doelling, D. R., Loeb, N. G., Keyes, D. F., Nordeen, M. L., Morstad, D., Nguyen, C., Wielicki, B. A., Young, D. F., and Sun, M.: Geostationary Enhanced Temporal Interpolation for CERES Flux Products, Journal of Atmospheric and Oceanic Technology, 30, 1072 – 1090, https://doi.org/10.1175/JTECH-D-12-00136.1, 2013.

Désalmand, F.: Observations of CCN concentrations south of the Sahara during a Dust Haze, Atmospheric Research, 21, 13–28, https://doi.org/10.1016/0169-8095(87)90014-7, 1987.

310 Errera, Q., Bennouna, Y., Schulz, M., Eskes, H., Basart, S., Benedictow, A., Blechschmidt, A.-M., Chabrillat, S., Clark, H., Cuevas, E., et al.: Validation report of the CAMS global Reanalysis of aerosols and reactive gases, years 2003-2020, Copernicus Atmosphere Monitoring Service (CAMS) report, https://doi.org/10.24380/8gf9-k005, 2021.

Forster, P., Storelvmo, T., Armour, K., Collins, W., Dufresne, J.-L., Frame, D., Lunt, D., Mauritsen, T., Palmer, M., Watanabe, M., Wild, M., and Zhang, H.: The Earth's Energy Budget, Climate Feedbacks, and Climate Sensitivity, in: Climate Change 2021: The Physical Science
315 Basis. Contribution of Working Group I to the Sixth Assessment Report of the Intergovernmental Panel on Climate Change, edited by Masson-Delmotte, V., Zhai, P., Pirani, A., Connors, S., Péan, C., Berger, S., Caud, N., Chen, Y., Goldfarb, L., Gomis, M., Huang, M., Leitzell, K., Lonnoy, E., Matthews, J., Maycock, T., Waterfield, T., Yelekçi, O., Yu, R., and Zhou, B., pp. 923–1054, Cambridge University Press, Cambridge, United Kingdom and New York, NY, USA, https://doi.org/10.1017/9781009157896.009, 2021.

Garimella, S., Huang, Y.-W., Seewald, J. S., and Cziczo, D. J.: Cloud condensation nucleus activity comparison of dry- and
320 wet-generated mineral dust aerosol: the significance of soluble material, Atmospheric Chemistry and Physics, 14, 6003–6019, https://doi.org/10.5194/acp-14-6003-2014, 2014.

Gasteiger, J. and Wiegner, M.: MOPSMAP v1.0: a versatile tool for the modeling of aerosol optical properties, Geoscientific Model Development, 11, 2739–2762, https://doi.org/10.5194/gmd-11-2739-2018, 2018.

Gryspeerdt, E., Quaas, J., Ferrachat, S., Gettelman, A., Ghan, S., Lohmann, U., Morrison, H., Neubauer, D., Partridge, D. G., Stier, P.,
325 Takemura, T., Wang, H., Wang, M., and Zhang, K.: Constraining the instantaneous aerosol influence on cloud albedo, Proceedings of the National Academy of Sciences, 114, 4899–4904, https://doi.org/10.1073/pnas.1617765114, 2017.

Gryspeerdt, E., Smith, T. W. P., O'Keeffe, E., Christensen, M. W., and Goldsworth, F. W.: The Impact of Ship Emission Controls Recorded by Cloud Properties, Geophysical Research Letters, 46, 12 547–12 555, https://doi.org/10.1029/2019GL084700, 2019.

Gryspeerdt, E., Goren, T., and Smith, T. W. P.: Observing the timescales of aerosol–cloud interactions in snapshot satellite images, Atmo-
330 spheric Chemistry and Physics, 21, 6093–6109, https://doi.org/10.5194/acp-21-6093-2021, 2021.

Gryspeerdt, E., McCoy, D., Crosbie, E., Moore, R. H., Nott, G. J., Painemal, D., Small-Griswold, J. D., Sorooshian, A., and Ziemba, L.: Cloud droplet number concentration, calculated from the MODIS (Moderate resolution imaging spectroradiometer) cloud optical properties retrieval and gridded using different sampling strategies, NERC EDS Centre for Environmental Data Analysis [data set], https://doi.org/10.5285/864a46cc65054008857ee5bb772a2a2b, 2022.

335 Hasekamp, O. P., Gryspeerdt, E., and Quaas, J.: Analysis of polarimetric satellite measurements suggests stronger cooling due to aerosol-cloud interactions, Nature Communications, 10, 5405, https://doi.org/10.1038/s41467-019-13372-2, 2019.

Humphries, R. S., Keywood, M. D., Ward, J. P., Harnwell, J., Alexander, S. P., Klekociuk, A. R., Hara, K., McRobert, I. M., Protat, A., Alroe, J., Cravigan, L. T., Miljevic, B., Ristovski, Z. D., Schofield, R., Wilson, S. R., Flynn, C. J., Kulkarni, G. R., Mace, G. G., McFarquhar, G. M., Chambers, S. D., Williams, A. G., and Griffiths, A. D.: Measurement report: Understanding the seasonal cycle of Southern Ocean

340 aerosols, Atmospheric Chemistry and Physics, 23, 3749–3777, https://doi.org/10.5194/acp-23-3749-2023, 2023.

IMO: IMO: Annex 15, Resolution MEPC.321(74) 2019 Guidelines for Port State Control Under MARPOL Annex VI Chapter 3, https://wwwcdn.imo.org/localresources/en/OurWork/Environment/Documents/MEPC.321(74).pdf, accessed on 4 March 2022, 2019.

Inness, A., Ades, M., Agustí-Panareda, A., Barré, J., Benedictow, A., Blechschmidt, A.-M., Dominguez, J. J., Engelen, R., Eskes, H., Flemming, J., Huijnen, V., Jones, L., Kipling, Z., Massart, S., Parrington, M., Peuch, V.-H., Razinger, M., Remy, S., Schulz, M., and Suttie, M.:

345 The CAMS reanalysis of atmospheric composition, Atmospheric Chemistry and Physics, 19, 3515–3556, https://doi.org/10.5194/acp-19-3515-2019, 2019.

Jayachandran, V. N., Varghese, M., Murugavel, P., Todekar, K. S., Bankar, S. P., Malap, N., Dinesh, G., Safai, P. D., Rao, J., Konwar, M., Dixit, S., and Prabha, T. V.: Cloud condensation nuclei characteristics during the Indian summer monsoon over a rain-shadow region, Atmospheric Chemistry and Physics, 20, 7307–7334, https://doi.org/10.5194/acp-20-7307-2020, 2020.

350 Jin, S., Ma, Y., Huang, Z., Huang, J., Gong, W., Liu, B., Wang, W., Fan, R., and Li, H.: A comprehensive reappraisal of long-term aerosol characteristics, trends, and variability in Asia, Atmospheric Chemistry and Physics, 23, 8187–8210, https://doi.org/10.5194/acp-23-8187-2023, 2023.

Kumar, P., Nenes, A., and Sokolik, I. N.: Importance of adsorption for CCN activity and hygroscopic properties of mineral dust aerosol, Geophysical Research Letters, 36, https://doi.org/https://doi.org/10.1029/2009GL040827, 2009.

355 McCoy, D. T., Bender, F. A.-M., Grosvenor, D. P., Mohrmann, J. K., Hartmann, D. L., Wood, R., and Field, P. R.: Predicting decadal trends in cloud droplet number concentration using reanalysis and satellite data, Atmospheric Chemistry and Physics, 18, 2035–2047, https://doi.org/10.5194/acp-18-2035-2018, 2018.

Moore, R. H., Karydis, V. A., Capps, S. L., Lathem, T. L., and Nenes, A.: Droplet number uncertainties associated with CCN: an assessment using observations and a global model adjoint, Atmospheric Chemistry and Physics, 13, 4235–4251, https://doi.org/10.5194/acp-13-4235-

360 2013, 2013.

O'Connor, F. M., Johnson, C. E., Morgenstern, O., Abraham, N. L., Braesicke, P., Dalvi, M., Folberth, G. A., Sanderson, M. G., Telford, P. J., Voulgarakis, A., Young, P. J., Zeng, G., Collins, W. J., and Pyle, J. A.: Evaluation of the new UKCA climate-composition model – Part 2: The Troposphere, Geoscientific Model Development, 7, 41–91, https://doi.org/10.5194/gmd-7-41-2014, 2014.

Paramonov, M., Kerminen, V.-M., Gysel, M., Aalto, P. P., Andreae, M. O., Asmi, E., Baltensperger, U., Bougiatioti, A., Brus, D., Frank,

365 G. P., Good, N., Gunthe, S. S., Hao, L., Irwin, M., Jaatinen, A., Juranyi, Z., King, S. M., Kortelainen, A., Kristensson, A., Lihavainen, H., Kulmala, M., Lohmann, U., Martin, S. T., McFiggans, G., Mihalopoulos, N., Nenes, A., O'Dowd, C. D., Ovadnevaite, J., Petäjä, T., Pöschl, U., Roberts, G. C., Rose, D., Svenningsson, B., Swietlicki, E., Weingartner, E., Whitehead, J., Wiedensohler, A., Wittbom, C.,

and Sierau, B.: A synthesis of cloud condensation nuclei counter (CCNC) measurements within the EUCAARI network, Atmospheric
Chemistry and Physics, 15, 12 211–12 229, https://doi.org/10.5194/acp-15-12211-2015, 2015.

370 Platnick, S., King, M., and Hubanks, P.: MODIS Atmosphere L3 Monthly Product, NASA MODIS Adaptive Processing System, Goddard
Space Flight Center [data set], https://doi.org/10.5067/MODIS/MYD08_M3.061, 2017a.

Platnick, S., Meyer, K. G., King, M. D., Wind, G., Amarasinghe, N., Marchant, B., Arnold, G. T., Zhang, Z., Hubanks, P. A., Holz, R. E., Yang,
P., Ridgway, W. L., and Riedi, J.: The MODIS Cloud Optical and Microphysical Products: Collection 6 Updates and Examples From Terra
and Aqua, IEEE Transactions on Geoscience and Remote Sensing, 55, 502–525, https://doi.org/10.1109/TGRS.2016.2610522, 2017b.

375 Popp, T., De Leeuw, G., Bingen, C., Brühl, C., Capelle, V., Chedin, A., Clarisse, L., Dubovik, O., Grainger, R., Griesfeller, J., Heckel, A.,
Kinne, S., Klüser, L., Kosmale, M., Kolmonen, P., Lelli, L., Litvinov, P., Mei, L., North, P., Pinnock, S., Povey, A., Robert, C., Schulz,
M., Sogacheva, L., Stebel, K., Stein Zweers, D., Thomas, G., Tilstra, L. G., Vandenbussche, S., Veefkind, P., Vountas, M., and Xue, Y.:
Development, Production and Evaluation of Aerosol Climate Data Records from European Satellite Observations (Aerosol_cci), Remote
Sensing, 8, https://doi.org/10.3390/rs8050421, 2016.

380 Pöhlker, M. L., Pöhlker, C., Quaas, J., Mülmenstädt, J., Pozzer, A., Andreae, M. O., Artaxo, P., Block, K., Coe, H., Ervens, B., Gallimore, P.,
Gaston, C. J., Gunthe, S. S., Henning, S., Herrmann, H., Krüger, O. O., McFiggans, G., Poulain, L., Raj, S. S., Reyes-Villegas, E., Royer,
H. M., Walter, D., Wang, Y., and Pöschl, U.: Global organic and inorganic aerosol hygroscopicity and its effect on radiative forcing, Nature
Communications, 14, 6139, https://doi.org/10.1038/s41467-023-41695-8, 2023.

Quaas, J., Arola, A., Cairns, B., Christensen, M., Deneke, H., Ekman, A. M. L., Feingold, G., Fridlind, A., Gryspeerdt, E., Hasekamp, O., Li,
385 Z., Lipponen, A., Ma, P.-L., Mülmenstädt, J., Nenes, A., Penner, J. E., Rosenfeld, D., Schrödner, R., Sinclair, K., Sourdeval, O., Stier, P.,
Tesche, M., van Diedenhoven, B., and Wendisch, M.: Constraining the Twomey effect from satellite observations: issues and perspectives,
Atmospheric Chemistry and Physics, 20, 15 079–15 099, https://doi.org/10.5194/acp-20-15079-2020, 2020.

Quaas, J., Jia, H., Smith, C., Albright, A. L., Aas, W., Bellouin, N., Boucher, O., Doutriaux-Boucher, M., Forster, P. M., Grosvenor, D., Jenk-
ins, S., Klimont, Z., Loeb, N. G., Ma, X., Naik, V., Paulot, F., Stier, P., Wild, M., Myhre, G., and Schulz, M.: Robust evidence for reversal
390 of the trend in aerosol effective climate forcing, Atmospheric Chemistry and Physics, 22, 12 221–12 239, https://doi.org/10.5194/acp-22-
12221-2022, 2022.

Redemann, J., Wood, R., Zuidema, P., Doherty, S. J., Luna, B., LeBlanc, S. E., Diamond, M. S., Shinozuka, Y., Chang, I. Y., Ueyama, R.,
Pfister, L., Ryoo, J.-M., Dobracki, A. N., da Silva, A. M., Longo, K. M., Kacenelenbogen, M. S., Flynn, C. J., Pistone, K., Knox, N. M.,
Piketh, S. J., Haywood, J. M., Formenti, P., Mallet, M., Stier, P., Ackerman, A. S., Bauer, S. E., Fridlind, A. M., Carmichael, G. R., Saide,
395 P. E., Ferrada, G. A., Howell, S. G., Freitag, S., Cairns, B., Holben, B. N., Knobelspiesse, K. D., Tanelli, S., L'Ecuyer, T. S., Dzambo,
A. M., Sy, O. O., McFarquhar, G. M., Poellot, M. R., Gupta, S., O'Brien, J. R., Nenes, A., Kacarab, M., Wong, J. P. S., Small-Griswold,
J. D., Thornhill, K. L., Noone, D., Podolske, J. R., Schmidt, K. S., Pilewskie, P., Chen, H., Cochrane, S. P., Sedlacek, A. J., Lang, T. J.,
Stith, E., Segal-Rozenhaimer, M., Ferrare, R. A., Burton, S. P., Hostetler, C. A., Diner, D. J., Seidel, F. C., Platnick, S. E., Myers, J. S.,
Meyer, K. G., Spangenberg, D. A., Maring, H., and Gao, L.: An overview of the ORACLES (ObseRvations of Aerosols above CLouds
400 and their intEractionS) project: aerosol–cloud–radiation interactions in the southeast Atlantic basin, Atmospheric Chemistry and Physics,
21, 1507–1563, https://doi.org/10.5194/acp-21-1507-2021, 2021.

Revell, L. E., Kremser, S., Hartery, S., Harvey, M., Mulcahy, J. P., Williams, J., Morgenstern, O., McDonald, A. J., Varma, V., Bird, L.,
and Schuddeboom, A.: The sensitivity of Southern Ocean aerosols and cloud microphysics to sea spray and sulfate aerosol production
in the HadGEM3-GA7.1 chemistry–climate model, Atmospheric Chemistry and Physics, 19, 15 447–15 466, https://doi.org/10.5194/acp-
405 19-15447-2019, 2019.

Rosenfeld, D., Kokhanovsky, A., Goren, T., Gryspeerdt, E., Hasekamp, O., Jia, H., Lopatin, A., Quaas, J., Pan, Z., and Sourde-val, O.: Frontiers in Satellite-Based Estimates of Cloud-Mediated Aerosol Forcing, Reviews of Geophysics, 61, e2022RG000 799, https://doi.org/10.1029/2022RG000799, 2023.

Ross, K. E., Piketh, S. J., Bruintjes, R. T., Burger, R. P., Swap, R. J., and Annegarn, H. J.: Spatial and seasonal variations in 410 CCN distribution and the aerosol-CCN relationship over southern Africa, Journal of Geophysical Research: Atmospheres, 108, https://doi.org/10.1029/2002JD002384, 2003.

Shen, Y., Virkkula, A., Ding, A., Luoma, K., Keskinen, H., Aalto, P. P., Chi, X., Qi, X., Nie, W., Huang, X., Petäjä, T., Kulmala, M., and Kerminen, V.-M.: Estimating cloud condensation nuclei number concentrations using aerosol optical properties: role of particle number size distribution and parameterization, Atmospheric Chemistry and Physics, 19, 15 483–15 502, https://doi.org/10.5194/acp-19-15483-415 2019, 2019.

West, R. E. L., Stier, P., Jones, A., Johnson, C. E., Mann, G. W., Bellouin, N., Partridge, D. G., and Kipling, Z.: The importance of vertical velocity variability for estimates of the indirect aerosol effects, Atmospheric Chemistry and Physics, 14, 6369–6393, https://doi.org/10.5194/acp-14-6369-2014, 2014.

Wood, R., Stemmler, J. D., Rémillard, J., and Jefferson, A.: Low-CCN concentration air masses over the eastern North Atlantic: Seasonality, 420 meteorology, and drivers, Journal of Geophysical Research: Atmospheres, 122, 1203–1223, https://doi.org/10.1002/2016JD025557, 2017.

Yu, L., Zhong, S., and Sun, B.: The Climatology and Trend of Surface Wind Speed over Antarctica and the Southern Ocean and the Implica-tion to Wind Energy Application, Atmosphere, 11, https://doi.org/10.3390/atmos11010108, 2020.